Dalton Transactions

ROYAL SOCIETY OF CHEMISTRY

PAPER

View Article Online
View Journal | View Issue



Cite this: *Dalton Trans.*, 2024, **53**, 2487

# Oxygen reduction reaction (ORR) in alkaline solution catalysed by an atomically precise catalyst based on a Pd(II) complex supported on multi-walled carbon nanotubes (MWCNTs). Electrochemical and structural considerations†

Valeria Monini,[a] Marco Bonechi, *[a] Carla Bazzicalupi, *[a] Antonio Bianchi,[a,b] Pietro Gentilesca,[a] Walter Giurlani,[a] Massimo Innocenti,[a,b] Arianna Meoli,[a] Giammarco Maria Romano[a] and Matteo Savastano *[b,c]

A new atomically precise, single-ion catalyst (MWCNT-LPd) for ORR (oxygen reduction reaction), consisting of a Pd(II) complex of a tetraazacycloalkane anchored on multiwalled carbon nanotubes, has been prepared through a supramolecular approach ensuring a uniform distribution of catalytic centres on the support surface. A tetraazacycloalkane was chosen to saturate the four coordination sites of the typical square planar coordination geometry of Pd(II) with the aim of ascertaining whether the metal ion must have free coordination sites to function effectively in the ORR or whether, as predicted by quantum mechanical calculations, the catalytic effect can be originated from an interaction of $O_2$ in the fifth coordinative position. The results clearly demonstrated that tetracoordination of Pd(II) does not influence its catalytic capacity in the ORR. Electrodes based on this catalyst show ORR performance very close to that of commercial Pt electrodes, despite the low Pd(II) content (1.72% by weight) in the catalyst. The onset potential ($E_{on}$) value and the half-wave potential ($E_{1/2}$) of the catalyst are, respectively, only 53 mV and 24 mV less positive than those observed for the Pt electrode and direct conversion of $O_2$ to $H_2O$ reaches 85.0%, compared to 89% of the Pt electrode. Furthermore, a preliminary galvanostatic test (simulating a working fuel cell at a fixed potential) showed that the catalyst maintains its efficiency continuing to produce water throughout the process (the average number of electrons exchanged over time per $O_2$ molecule remains close to 4).

Received 24th November 2023,
Accepted 21st December 2023

DOI: 10.1039/d3dt03947a

rsc.li/dalton



## Introduction

The oxygen reduction reaction (ORR) is one of the most important reactions both in life processes (*e.g.* aerobic respiration) and in artificial energy conversion systems such as fuel cells.[1,2] The ORR that occurs at the fuel cell cathode is a sluggish process, so it needs to be catalysed for profitable use and Pt-based electrocatalysts are the primary choice for this purpose due to their high catalytic performance.[3–6]

Unfortunately, the scarcity and the high price of this precious metal make Pt-based electrocatalysts very expensive, too expensive to find a daily application in support of human activities that require an energy supply. Nonetheless, fuel cells are an important clean alternative to internal combustion engines that burn fossil fuels and generate greenhouse gases, in addition to a multitude of pollutants,[7] and accordingly the search for alternative catalysts is garnering strong consideration. To replace platinum and other platinum group metals of similar cost, several strategies are being studied that make use of electrocatalysts based on less expensive non-noble transition metals[8–12] or employ non-metallic[12–16] or atomically precise[17–20] electrodes. Atomically precise electrocatalysts are of special interest due to their high atomic utilization efficiency, special electronic structure and homogeneous distribution of active centres.[17–20]

Two main pathways are possible for ORR in aqueous solutions: (i) a 4-electron (4e) reduction of $O_2$ to $H_2O$ (or $OH^-$) in

[a]*Department of Chemistry "Ugo Schiff", University of Florence, Via della Lastruccia 3-13, 50019 Sesto Fiorentino, Italy.*
*E-mail: marco.bonechi@unifi.itCarla, carla.bazzicalupi@unifi.it*
[b]*National Interuniversity Consortium of Materials Science and Technology (INSTM), Research Unit of Florence, Via G. Giusti 9, 50121 Florence, Italy.*
*E-mail: matteo.savastano@uniroma5.it*
[c]*Department of Human Sciences for the Promotion of Quality of Life, University San Raffaele Roma, Via di Val Cannuta 247, 00166 Rome, Italy*

†Electronic supplementary information (ESI) available: Crystal data, refinement parameters, and selected bond distances and angles; superimposition of ligands and complexes in crystal structures; MD simulation of the graphene–$[Pd(H_2L)]^{2+}$ interaction; SEM, SEM-EDS and XPS data; CV and LSV diagrams; galvanostatic RRDE data. CCDC 2309459–2309463. For ESI and crystallographic data in CIF or other electronic format see DOI: https://doi.org/10.1039/d3dt03947a

acidic (or alkaline) solutions and (ii) a 2-electron (2e) reduction of $O_2$ to $H_2O_2$, (or $HO_2^-$) in acidic (or alkaline) solutions. Although the electrocatalytic production of hydrogen peroxide ($H_2O_2$) is gaining increasing interest, as $H_2O_2$ is considered a green oxidant,[21–23] the formation of $H_2O_2$ in fuel cells is deleterious as this undesired side reaction leads to loss of energy and can cause serious damage to cell catalysts and membranes.[24,25] Nevertheless, $H_2O_2$ can be converted into water *via* another 2e reaction.

We recently reported that two atomically precise, single-ion Pd(II) catalysts constructed *via* supramolecular (non-covalent) decoration of multiwalled carbon nanotubes (MWCNTs) with Pd(II) tetraaza-macrocyclic complexes have demonstrated great potential to accelerate the ORR.[26] These catalysts, having a very low Pd load (5%), exhibited excellent half-cell PGM mass activity, exceeding state-of-the-art reference goals of the time,[27] onset potential ($E_{on}$) values comparable to or better than that of a commercial Pt electrode and a nearly unique (90% or above) 4e process, leading to direct production of $H_2O$. The macrocyclic ligands employed in this study[26] and in successive studies[28,29] to append Pd(II) ions to MWCNTs were selected with the dual goal of ensuring robust metal ion coordination, to prevent loss of catalytic centres during electrode operation, and involving a metal ion in the coordination of up to three nitrogen atoms of the ligand, thus avoiding saturation of the square planar coordination sphere typical of Pd(II) with macrocycle's donor atoms, in the belief that the presence of at least one labile donor is beneficial for the proper functioning of the catalysts.[30–32] Accordingly, our Pd(II) complexes contained one labile $Cl^-$ ligand coordinated to the metal ion. While this fast exchangeable ancillary ligand ($Cl^-$) was fundamental for Sonogashira cross-coupling reactions,[33,34] which requires the simultaneous coordination to Pd(II) of two different reagent molecules, theoretical calculations[35] showed that this is not mandatory for ORR, as $O_2$ is able to form an apical bond with the metal centre.

To find an experimental verification of these theoretical results, which would greatly simplify the design of atomically precise catalysts based on $d^8$ metal ions by eliminating the need to build unsaturated environments around them, we prepared a new catalyst containing Pd(II) ions blocked into the $N_4$ square planar coordination environment offered by a cyclen-based (cyclen = 1,4,7,10-tetraaza-cyclododecane) ligand ($H_2L$, Fig. 1). The Pd(II) complex of $H_2L$ was anchored on MWCNTs *via* spontaneous adsorption under environmentally friendly conditions (water, room temperature, unprotected atmosphere) and the resulting MWCNT-LPd hybrid material was tested toward the ORR in alkaline media.

# Experimental

## Materials

All starting materials were high purity compounds purchased from commercial sources and were used without further purification. 6-Amino-3,4-dihydro-3-methyl-2-methoxy-5-nitroso-4-oxopyrimidine ((**3**), Fig. 1) was prepared according to a literature procedure.[36] Graphitized MWCNTs (99.9% C, outer diameter 8–15 nm, inner diameter 3–5 nm, specific surface area 117 $m^2\ g^{-1}$) were purchased from NanoAmor (Texas, USA).

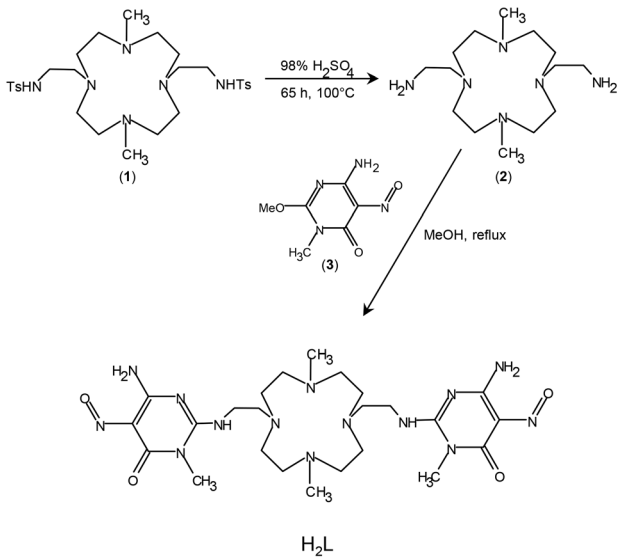


Fig. 1 The synthetic procedure adopted to prepare the $H_2L$ ligand.

**Synthesis of $H_2L$.** The procedure adopted for the synthesis of $H_2L$ is schematically represented in Fig. 1. Compound (**1**) was prepared as previously reported.[37] The hydrolysis of (**1**) to give (**2**) was conducted by dissolving 2.5 g (4.2 mmol) of (**1**) in 11 $cm^3$ of concentrated (98%) $H_2SO_4$ and heating the solution at 100 °C for 65 hours. The resulting solution was then cooled at room temperature and slowly poured into 200 $cm^3$ of cooled diethyl ether. The white solid thus formed was filtered, washed with diethyl ether and dried under reduced pressure at room temperature. The dried solid was then dissolved in 30 $cm^3$ of 2 M NaOH solution and extracted with $CHCl_3$ (5 × 50 $cm^3$). The organic phase was dried over anhydrous $Na_2SO_4$ and successively evaporated to dryness under reduced pressure. The oily residue was dried for 48 hours at room temperature under reduced pressure in the presence of solid NaOH as a desiccant. Yield 1.20 g (4.19 mmol), 99.8%. $^1H$ NMR (400 MHz, $CDCl_3$): $\delta$ 2.19 (s, 6H), 2.43 (t, 4H), 2.49–2.54 (m, 16H), 2.72 (t, 4H).

0.50 g (1.75 mmol) of (**2**) were dissolved in 150 $cm^3$ of methanol and 0.67 g (3.67 mmol) of (**3**) were added to the resulting solution in small portions, under stirring, at room temperature. The mixture was then refluxed for 3 hours to obtain a solution that was kept at room temperature overnight. The solid formed was filtered, washed with methanol and dried under reduced pressure at room temperature. Another batch of the same compound was obtained from the mother liquor. The mother liquor was treated with 10 drops of 37% $NH_3$ aqueous solution to convert the excess of (**3**) into its insoluble derivative 2,4-diamino-1-methyl-5-nitroso-6-oxopyrimidine. The solid formed upon standing in a fridge overnight

 

was removed by filtration, and the resulting solution was evaporated to dryness under reduced pressure. The remaining solid compound was dried at room temperature under reduced pressure. Overall yield 0.70 g (1.12 mmol), 64%. $^1$H NMR (400 MHz, $CDCl_3$): $\delta$ 2.16 (s, 6H), 2.99 (m, 8H), 3.06 (m, 4H), 3.15 (m, 4H), 3.28 (m, 4H), 3.34 (m, 3H), 3.47 (m, 4H), 3.80 (t, 4H). Elem Anal. Calcd (%) for $C_{24}H_{42}N_{14}O_4$: C 48.80, H 7.17, N 33.20. Found: C 48.68, H 7.13, N 33.08.

**Synthesis of $(H_3L)(H_4L)(ClO_4)_3\cdot 11H_2O$.** Crystals of this compound suitable for XRD analysis were obtained by slow evaporation at room temperature of a solution of $H_2L$ (20.0 mg, 0.032 mmol) with the pH adjusted to 7 by addition of $HClO_4$. Yield 16.0 mg, 57%. Elem Anal. Calcd (%) for $C_{48}H_{109}N_{28}O_{31}Cl_3$: C 34.30; H 6.54; N 23.33. Found: C 33.99; H 6.60; N 23.15.

**Synthesis of $(H_5L)(ClO_4)_3\cdot 2H_2O$.** Crystals of this compound suitable for XRD analysis were obtained by slow evaporation at room temperature of a solution of $H_2L$ (20.0 mg, 0.032 mmol) with the pH adjusted to 2.5 by addition of $HClO_4$. Yield 19.4 mg, 63%. Elem Anal. Calcd (%) for $C_{24}H_{49}N_{14}O_{18}Cl_3$: C 31.07; H 5.32; N 21.13. Found: C 29.94; H 5.39; N 21.04.

**Synthesis of $[Cu(H_2L)](ClO_4)_2\cdot 10.46H_2O$.** $H_2L$ (20.0 mg, 0.032 mmol) and $Cu(ClO_4)_2\cdot 6H_2O$ (11.9 mg, 0.032 mmol) were dissolved in a minimum amount of boiling methanol. Crystals of $[Cu(H_2L)](ClO_4)_2\cdot 10.46H_2O$ suitable for XRD analysis were obtained by slow evaporation of this solution at room temperature. Yield 13.2 mg, 38%. Elem Anal. Calcd (%) for $C_{24}H_{64.92}N_{14}O_{23.46}Cl_2Cu$: C 27.20; H 6.18; N 18.51. Found: C 27.29; H 6.23; N 18.59.

**Synthesis of $[Cu(H_2L)Cl]Cl\cdot 3H_2O$.** $H_2L$ (20.0 mg, 0.032 mmol) and $CuCl_2$ (4.3 mg, 0.032 mmol) were dissolved in 5 cm$^3$ of boiling water. Crystals of $[Cu(H_2L)Cl]Cl\cdot 3H_2O$ suitable for XRD analysis were obtained by slow evaporation of this solution at room temperature. Yield 10.6 mg, 41%. Elem Anal. Calcd (%) for $C_{24}H_{48}N_{14}O_7Cl_2Cu$: C 36.99; H 6.21; N 25.17. Found: C 36.84; H 6.30; N 25.04.

**Synthesis of $[Pd(1)]Cl_2\cdot 4.5H_2O$.** (**1**) (20.0 mg, 0.032 mmol) and $K_2PdCl_4$ (10.4 mg, 0.031 mmol) were dissolved in 5 cm$^3$ of boiling acetonitrile upon addition of a minimum amount of water necessary to dissolve the metal salt. Crystals of $[Pd(1)]Cl_2\cdot 4.5H_2O$ suitable for XRD analysis were obtained by slow evaporation of this solution at room temperature. Yield 15.8 mg, 58%. Elem Anal. Calcd (%) for $C_{28}H_{55}N_6O_{8.5}S_2Cl_2Pd$: C 39.42; H 6.50; N 9.85. Found: C 39.36; H 6.41; N 9.76.

### Potentiometric measurements

The protonation constants of $H_2L$ were determined by means of potentiometric (pH-metric) titrations in 0.1 M $NMe_4Cl$ aqueous solution at 298.1 ± 0.1 K using an automated apparatus and a procedure previously described.[38] The acquisition of the emf data was performed with the computer program PASAT.[39,40] The combined electrode (Metrohm 6.0262.100) was calibrated as a hydrogen-ion concentration probe by titration of known amounts of HCl with $CO_2$-free NaOH solutions and determining the equivalent point by Gran's method,[41] which gives the standard potential, $E^\circ$, and the ionic product of water ($pK_w$ = 13.83(1) in 0.1 M $NMe_4Cl$ at 298.1 K). The stability constants were calculated from the potentiometric data by means of the computer program HYPERQUAD.[42] The concentration of $H_2L$ was about $1 \times 10^{-3}$ M in all experiments and the studied pH range was 2.0–11.5. Three measurements were performed and used to determine the protonation constants.

### Preparation of the catalyst

The MWCNT-LPd catalyst was prepared in two steps according to a previously reported successful procedure:[43] (i) adsorption of $H_2L$ onto the surface of MWCNTs in water *via* a π–π interaction of the hydrophobic pyrimidine residue of the ligand with the graphene surface of the nanotubes and (ii) decoration of the macrocyclic ligand moiety with coordinated Pd(II) ions.

First, 100 mg of MWCNTs were suspended in 50 cm$^3$ of a 1 mM solution of the ligand at pH 8.5. The suspension was sonicated for a few minutes and successively kept under stirring for 6 days at room temperature. The solid was then recovered by filtration and dried under reduced pressure, at room temperature, and in the presence of a desiccant (NaOH) until constant weight. The amount of ligand adsorbed (0.174 mmol g$^{-1}$) was determined by measuring the concentration of ligand remaining in the solution by means of UV spectroscopy (Fig. S1†). The resulting solid was successively suspended in water (1 mg cm$^{-3}$ of water, pH 5), and the suspension was kept under stirring at room temperature for 6 days. The solid was recovered and dried under reduced pressure, at room temperature, and in the presence of a desiccant (NaOH) until constant weight. The amount of ligand remaining on the MWCNTs (0.162 mmol g$^{-1}$) was determined by measuring the concentration of the ligand desorbed into the solution by means of UV spectroscopy (Fig. S1†).

In the second step, 50 mg of the MWCNT-L material, obtained in the first step, was suspended in 50 cm$^3$ of a solution, at pH 5, containing one equivalent of $K_2PdCl_4$ (relative to the ligand) and the resulting suspension was kept under stirring at room temperature. After 6 days, all metal ions had been adsorbed, as shown by the UV spectrum of the filtered suspension, which corresponds to the formation of a MWCNT-LPd catalyst containing 1.72% of Pd by weight. The MWCNT-LPd catalyst was recovered by filtration, washed with water and dried under reduced pressure, at room temperature, and in the presence of a desiccant (NaOH) until constant weight.

### Electrochemical measurement and modified electrodes' preparation

All the electrochemical measurements, cyclic voltammetry (CV) and linear sweep voltammetry (LSV) experiments, were performed with an AUTOLAB PGSTAT12 using NOVA software from Metrohm Autolab and a modulated speed rotator (MSR) 636A from Pine Instrument.

Electrochemical measurements were performed using a three-electrode cell. The reference electrode was an Ag/AgCl/sat. KCl electrode with a potential of +197 mV with respect to the normal hydrogen electrode (NHE). In the following, all potential values will be referred to the Ag/AgCl/saturated KCl reference electrode (RE), unless otherwise specified. The

counter electrode was a platinum wire, and the working electrode was a ring-disk electrode from Pine Instrument Co. consisting of a glassy carbon (GC) disk insert (∅ = 5.5 mm; $A$ = 0.238 $cm^2$) and a Pt ring ($\varnothing_{inner}$ = 6.50 mm, $\varnothing_{outer}$ = 8.50 mm, $A$ = 0.236 $cm^2$) with a theoretical collection efficiency ($N$) of 38.3%.

Rotating ring disk electrode (RRDE) experiments were performed in a glass cell filled with 0.1 M KOH solution. Nitrogen was used to achieve an oxygen-free solution (15 minutes of bubbling) while oxygen was used to obtain an oxygen-saturated electrolyte solution (20 min).

RRDE working electrodes were mechanically polished with 0.05 μm alumina and sonicated for five minutes in milliQ water. The Pt ring electrode was electropolished by scanning the potential at 100 mV $s^{-1}$ between −0.20 and +1.15 V in a 0.5 M $H_2SO_4$ solution until a reproducible curve was obtained.[44] Activation of the working electrode was confirmed in a 1 mM $K_3Fe(CN)_6$ solution in 0.1 M KCl by recording CVs in the −0.3 to +0.7 V potential range at 10 mV $s^{-1}$ scan rate; the typical $\Delta E_p$ for an activated electrode is very close to 60 mV.[45]

Immobilization of the catalysts onto the GC disk working electrode was achieved by preparing an ink consisting of MWCNT-LPd dispersed in a polymeric membrane (Nafion®). Samples were prepared according to reported procedures.[28,29,46] An appropriate amount of samples (2 mg) was dispersed in 52 μL of water, 32 μL of ethanol and 23 μL of a 5% Nafion® solution. The composition of wet ink was as follows: catalyst 2%, water 52%, EtOH 26% and Nafion® 20%. The resulting ink was sonicated for 30 min and drop-cast onto the glassy carbon disk electrode (10 μL). The modified GC electrode was then dried at room temperature.

Cyclic voltammograms were obtained by scanning the potential between +0.2 and −0.75 V at a potential scan rate of 5 mV $s^{-1}$. Linear sweep voltammograms were obtained at a rotation rate of 1600 rpm and a scan rate of 5 mV $s^{-1}$, in the potential range from +0.1 to −0.70 V for the modified GC electrode while the Pt ring electrode was held at +0.50 V. The ring current was recorded simultaneously with the disk current.

RRDE galvanostatic analysis at 1600 rpm and a selected potential value of −0.6 V (for the modified GC disk electrode) and +0.50 V for the Pt ring was performed within a 600 s framework.

RRDE calibration experiment was performed to determine the experimental collection efficiency ($N = I_{ring}/I_{disk}$) of the ring-disk, recording LSV at 1600 rpm of a oxygen-free $K_3Fe(CN)_6$ solution (1 mM) in 0.1 M KCl at a scan rate of 5 mV $s^{-1}$ in the potential range from +0.60 V to −0.60 V (for the modified GC disk) and applying a constant potential of +0.6 V at the ring.[47] The electron transfer number exchanged per $O_2$ molecule ($n$) occurring during the ORR process was calculated using the equation $n = 4I_{disk}/(I_{disk} + I_{ring}/N)$.[48,49]

A commercial Pine Instrument electrode consisting of a Pt disk insert (∅ = 5.5 mm; $A$ = 0.238 $cm^2$) and a Pt ring ($\varnothing_{inner}$ = 6.50 mm, $\varnothing_{outer}$ = 8.50 mm, $A$ = 0.236 $cm^2$) with a theoretical collection efficiency ($N$) of 38.3% was employed to benchmark the performance of the materials presented in this report.

### Spectrophotometric measurements

UV-vis absorption spectra were recorded at 298 K by using a Jasco V-670 spectrophotometer. The UV (vis) spectra of $H_2L$ were recorded in the pH range of 0.80–12.01 (0.78–12.15) with an $H_2L$ concentration of $1.80 \times 10^{-5}$ M ($1.95 \times 10^{-3}$ M). The UV-vis spectra of the Pd(II) complex were recorded in the pH range of 2.32–9.12 with $H_2L$ and Pd(II) (as $K_2PdCl_4$) concentrations of $1.80 \times 10^{-5}$ M. Mother solutions containing the ligand and the metal ions (concentrations given above) were prepared at pH 4, to avoid formation of metal hydroxides/oxides, and allowed to equilibrate for one day. Aliquots of these solutions were separated and their pH was adjusted to different values. Equilibration of these solutions was checked daily by means of UV-vis spectroscopy until invariance of the recorded spectra was reached (6 days). The recorded pH values of solutions were measured after equilibrium was reached.

### NMR spectroscopy

$^1H$ NMR spectra (400 MHz) in $D_2O$ solution were recorded at 298 K on a 400 MHz Bruker Avance III spectrometer.

### XPS analysis

MWCNT-LPd was fixed on a sample holder dropcasting a water dispersion onto a gold substrate and dried under a flow of $N_2$. The samples were then introduced into the ultra-high vacuum (UHV) chamber of the instrument. X-ray photoelectron spectroscopy (XPS) spectra were recorded while using Al Kα radiation and a pass energy of 44 eV for XPS survey and 22 eV for high resolution XPS spectra, using previously reported instrumentation and methods, namely using a model TA10 X-ray source and a model HA100 hemispherical analyser (VSW Scientific Instrument Limited, Manchester, UK) with a 12 channel detector. The C 1s transition at 284.8 eV was used as a reference for obtaining the heteroatom binding energies.[50,51] The collected data were analysed using the dedicated software CasaXPS (version 2.3.16Dev52). The background was subtracted using Shirley's method[52] and the peaks were fitted using mixed Gaussian–Lorentzian components.

### SEM analysis

SEM micrographs were obtained with a Hitachi SU3800 scanning electron microscope equipped with an UltimMax Oxford instrument detector (Oxford Instruments, Wiesbaden, Germany) and AZtecLive software (Oxford Instruments NanoAnalysis, Abingdon, United Kingdom). X-ray elemental mapping was carried out at 5 kV acceleration voltage and 10 mm working distance. MWCNT samples were fixed on the surface of conductive tape for SEM analysis.

### Crystal structure determination of $(H_5L)(ClO_4)_3{\cdot}2H_2O$, $(H_3L)(H_4L)(ClO_4)_3{\cdot}11H_2O$, $[Cu(H_2L)(H_2O)](ClO_4)_2{\cdot}10.46H_2O$, $[Cu(H_2L)Cl]Cl{\cdot}3H_2O$ and $[Pd(1)]Cl_2{\cdot}4H_2O$

A yellow crystal ($(H_5L)(ClO_4)_3{\cdot}2H_2O$), a violet crystal ($(H_3L)(H_4L)(ClO_4)_3{\cdot}11H_2O$), a blue crystal ($[Cu(H_2L)(H_2O)](ClO_4)_2{\cdot}10.46H_2O$), a dark blue crystal ($[Cu(H_2L)Cl]Cl{\cdot}3H_2O$) and a yellow crystal

 

([Pd(**1**)]$Cl_2$·4$H_2O$) were used for X-ray diffraction analyses. A summary of the crystallographic data is reported in Table S1.† In the case of the compound [Pd(**1**)]$Cl_2$·4$H_2O$, reflections were recorded up to $2\theta$ = 98° (1 Å), due to the significant lowering of intensity with increasing $\theta$ value. However, the reached resolution and the observed reflections/refined parameter ratio, about 8, ensure that the overall geometries of the complexes are confidently defined. The integrated intensities were corrected for Lorentz and polarization effects and an empirical absorption correction (SADABS)[53] was applied. Crystal structures were resolved by direct methods (SHELXT)[54] and refinements were performed by means of full-matrix least-squares using SHELXL Version 2019/3.[55] Non-H atoms were anisotropically refined. H atoms were introduced as riding atoms with the thermal parameter calculated in agreement with the linked atom. Some of the water hydrogen atoms and the ionisable hydrogen atoms, such as the amidic hydrogens of [Cu($H_2$L)($H_2O$)]($ClO_4$)$_2$·10.46$H_2O$, [Cu($H_2$L)Cl]Cl·3$H_2O$ and [Pd(**1**)]$Cl_2$·4$H_2O$ or the acidic hydrogen on the nitroso group of (($H_5$L)($ClO_4$)$_3$·2$H_2O$), were located in the Fourier difference maps, included in the calculations and freely refined. The amidic nitrogen atoms that were not localized in the Fourier difference map were always introduced as riding atoms with the thermal parameter calculated in agreement with the linked atom, with the exception of one of the Pd(II) complexes. The not localized water H atoms were not introduced in the calculations. Molecular plots were obtained using the software CCDC Mercury.[56]

## Results and discussion

The choice of 6-amino-3,4-dihydro-3-methyl-5-nitroso-4-oxopyrimidine as the anchor group to fix the Pd(II) complex on the surface of the MWCNTs was made considering the ability of pyrimidine residues to adhere with the arene centres of graphene surfaces, through the formation of strong π–π stacking interactions, giving rise to very stable, non-covalently assembled, hybrid materials which are suitable for successive functionalization with metal ions.[57] This route has already been proven to be effective for the preparation of robust single-ion Pd(II) catalysts.[26,28,29,33,34]

Nevertheless, before proceeding to verify the efficiency of a new catalyst, it is advisable to verify its ability to resist the conditions under which it will be used. The robustness of our single-ion catalyst (MWCNT-LPd) is principally determined by its resistance toward the loss of catalytic metal centres that might occur through two main processes: demetallation of the complex unit and detachment of the metal complex linked to MWCNTs. For similar catalysts, some demetallation of the complex unit is sometimes observed during the processes for which they are intended. However, this often occurs by reduction of Pd(II) to Pd(0), with the formation of Pd nanoparticles which can have their own catalytic activity and therefore the catalyst continues to be efficient.[28,33,34,43–45] Instead, detachment of the metal complex from the catalyst causes the loss of catalytic activity. The use of a macrocyclic ligand to bind Pd(II) ensures good resistance of the complex toward demetallation, both thermodynamically and kinetically. This is particularly true when the macrocycle fulfils the square-planar environment of Pd(II), as in our case, but there is a risk that the absence of readily available coordination positions on Pd(II) could be deleterious for the catalyst efficiency. The verification of this possibility is the main objective of the present study.

A screening of complex stability in solution over a wide pH range (see below) is preliminary to any other study to rule out pH-promoted demetallation effects that might occur, in acidic solutions, due to competition of ligand protonation with metal coordination and, in alkaline media, for the formation of insoluble metal hydroxides or oxides. A spectrophotometric study (UV-vis) was performed to address this aspect (see below).

Another crucial point is the effectiveness of the anchor group in ensuring a stable attachment of the complex to the surface of the carbon support (MWCNTs). The pyrimidine group used for our catalyst has proven effective for various catalytic processes, despite the non-covalent nature of the interaction with the carbon surface.[28,33,34,44–47] In this respect, the presence of two such anchor groups in $H_2$L should provide greater stability to the catalyst.[29] Nevertheless, for a stable attachment on the support surface, it is important that the ligand and the complex have an appropriate conformation for a correct "landing" on the support surface during the absorption processes. This means that, in the most stable conformations, both anchor groups should remain on the same side of the macrocyclic ring to avoid energy costs for conformational rearrangements or the possibility of only one anchor group adhering to the support surface. Since the construction of the catalyst occurs in two steps, first the adsorption of the ligand and subsequently the coordination of Pd(II), it is important to address this conformational issue both for the free ligand and for the metal complex. Concerning the free (not complexed) ligand, encouraging information was obtained from crystal structures of various protonated ligand forms (see below). Instead, despite our efforts, we were not able to obtain crystals of the Pd(II) complex suitable for XRD analysis. Crystallographic information was however obtained for the Cu(II) complex of $H_2$L and for the Pd(II) complex of the di-tosylated precursor (**1**) (Fig. 1) which is structurally rather similar to $H_2$L.

As we will see later, the results demonstrate that both the ligand and its metal complex have the requisites for the formation of a robust catalyst, as indeed it has been proven to be a property which usefully complements its high catalytic efficiency in the ORR.

### Ligand protonation and Pd(II) complexation in solution

$H_2$L contains two acidic groups that can undergo deprotonation (the NH groups of the bridges connecting the pyrimidine residues to the macrocycle) and six basic, protonable groups (the 4 macrocyclic N atoms and the two pyrimidine nitroso groups). Potentiometric (pH-metric) titrations performed in

aqueous solution (in 0.1 M $NMe_4Cl$, 298.1 ± 0.1 K) accounted for only one deprotonation and four protonation equilibria involving $H_2L$ in the pH range of 2–11.5. The relevant equilibrium constants are reported in Table 1.

Information on the protonation/deprotonation sites was obtained from the UV-vis spectra recorded at different pHs (Fig. 2a and b) as the pyrimidine chromophore is very sensitive to these processes. As can be seen, significant spectral variations are observed below pH 3 and above pH 11 when $H_5L^{3+}$ and $H_6L^{4+}$ (pH < 3) and $HL^-$ (pH > 11) are formed (Fig. 2c). Consequently, we can deduce that the formation of $H_5L^{3+}$ and $H_6L^{4+}$ involves, respectively, the protonation of one and two nitroso groups of the pyrimidine residues, while the formation of $HL^-$ takes place with deprotonation of one NH group of a bridge connecting a pyrimidine residue to the macrocycle. In the intermediate pH region (3–11), the spectra are poorly affected by the protonation equilibria (Fig. 2), indicating that they do not involve the pyrimidine chromophores but the macrocyclic unit. That is, in $H_3L^+$ and $H_4L^{2+}$, one and two N atoms of the macrocycle are respectively protonated. This protonation/deprotonation pattern is in agreement with the behaviour previously found for similar molecules,[28,33,34,48,49] and it is also consistent with the crystal structures of $(H_5L)(ClO_4)_3{\cdot}2H_2O$ and $(H_3L)(H_4L)(ClO_4)_3{\cdot}11H_2O$, determined by XRD, which show that single- and double-protonation of the macrocyclic ring in $H_3L^+$, $H_4L^{2+}$ and $H_5L^{3+}$ occur at the methylated nitrogen atoms and one nitroso group is protonated in $H_5L^{3+}$ (see below). In summary, in the pH range of 2–11.5, only one NH group of the bridges connecting the pyrimidine residues to the macrocycle undergoes deprotonation (the second one is expected to deprotonate at higher pH), both nitroso groups protonate and the macrocycle unit is involved in only two protonation equilibria (two of the amine groups remain unprotonated).

The formation of Pd(II) complexes with $H_2L$ was followed by means of UV-vis absorption spectroscopy. The complexation reaction is slow; it takes 6 days to reach the invariance of the recorded spectra at pH 4. The UV-vis spectra at different pH values (Fig. 3a and b) were recorded using a solution of the complex formed at pH 4 after changing its pH and monitoring the achievement of equilibrium by UV-vis spectroscopy. The pH attributed to each spectrum was measured once equilibration was achieved. A comparison of these spectra with the spectra of the metal-free ligand (Fig. 3c) shows that the Pd(II) complex is already formed in very acidic solutions (pH 2) and is preserved in alkaline media. The spectra of the complex remained unchanged for several weeks providing evidence of the long-lasting robustness of the complex under different pH conditions.

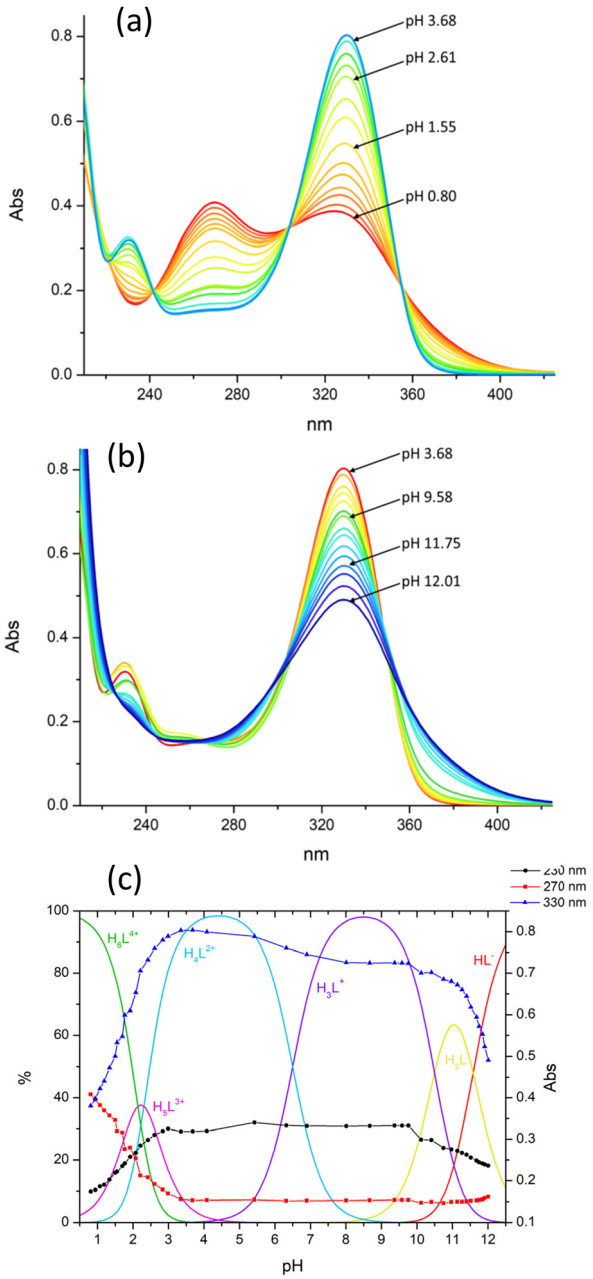


**Fig. 2** UV-Vis absorption spectra of $H_2L$ in the pH ranges 0.8–3.68 (a) and 3.68–12.01 (b). (c) Variation with pH of the 230 nm, 270 nm and 330 nm absorbances superimposed to the distribution diagram of the species formed by $H_2L$. $[H_2L] = 1.8 \times 10^{-5}$ M.

**Table 1** Equilibrium constants for protonation/deprotonation equilibria involving $H_2L$ in aqueous 0.1 M $NMe_4Cl$ solution, at 298.1 ± 0.1 K, in the pH range of 2–11.5. Values in parentheses are standard deviations on the last significant figures

| Equilibrium | log *K* |
|---|---|
| $HL^- + H^+ = H_2L$ | 11.58(2) |
| $H_2L + H^+ = H_3L^+$ | 10.50(2) |
| $H_3L^+ + H^+ = H_4L^{2+}$ | 6.40(8) |
| $H_4L^{2+} + H^+ = H_5L^{3+}$ | 2.31(8) |
| $H_5L^{3+} + H^+ = H_6L^{4+}$ | 2.14(8) |

## Crystallographic study

Four crystal structures for the ligand, $H_2L$ ($(H_5L)(ClO_4)_3{\cdot}2H_2O$, $(H_3L)(H_4L)(ClO_4)_3{\cdot}11H_2O$, $[Cu(H_2L)(H_2O)](ClO_4)_2{\cdot}10.46H_2O$

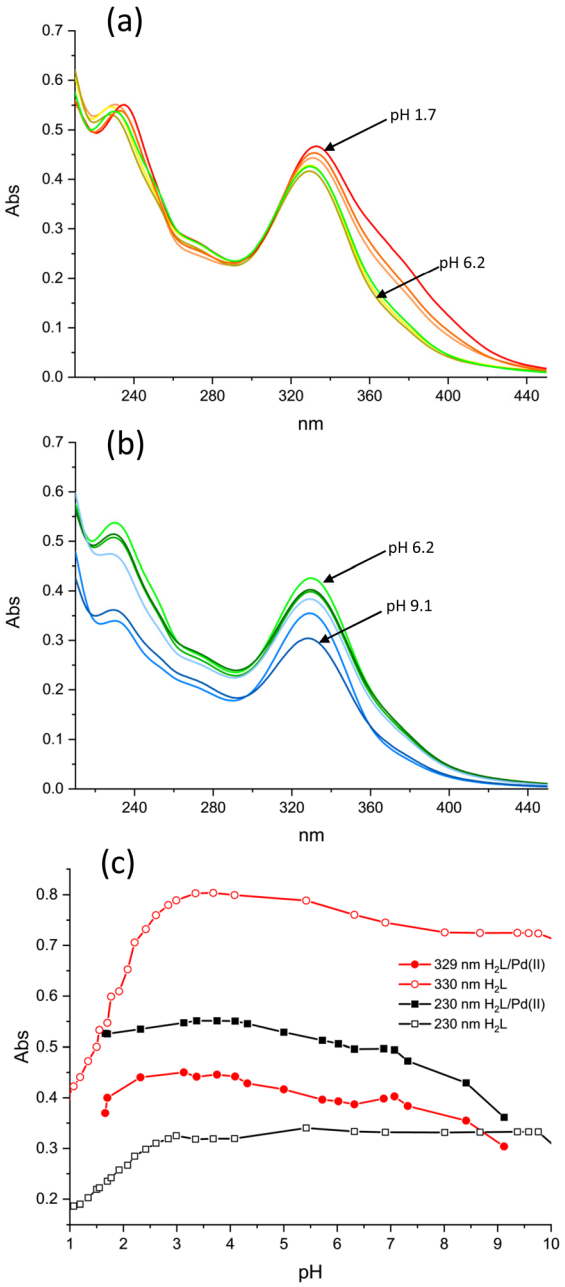


**Fig. 3** UV-Vis absorption spectra of the $H_2L$/Pd(II) system in the pH ranges 1.7–6.2 (a) and 6.2–9.1 (b). (c) Variation with pH of the 230 nm and 330 nm absorbances. $[H_2L] = [Pd(II)] = 1.8 \times 10^{-5}$ M.

and $[Cu(H_2L)Cl]Cl{\cdot}3H_2O$), and one crystal structure for the ditosylated molecule (**1**) ($[Pd(\mathbf{1})]Cl_2{\cdot}4H_2O$) were obtained and analysed.

The ORTEP-like drawings for the two protonated ligand forms and for the two Cu(II) complexes are shown in Fig. 4. The small macrocyclic moiety is quite rigid and in all structures assumes the same [3333] conformation,[58] which features all nitrogen atoms in *endo* conformation, with convergent lone pairs, and *gauche* dihedrals for the C–C ethylenic bonds. As a consequence, the acidic hydrogen atoms of the two metal-free structures (Fig. 4a and b), which were localized on the methylated nitrogen atoms using the Fourier difference maps, point towards a water molecule, with which they form H-bonds, located approximately above the centre of the macrocyclic ring. Further H-bonds are formed by this water molecule with the arms of symmetry related ligand molecules. Notably, macrocyclic rigidity prevents conformational changes when one $H^+$ ion is added to $H_3L^+$ to give $H_4L^{2+}$, as observed in $(H_3L)(H_4L)(ClO_4)_3{\cdot}11H_2O$. Overall, the two cations ($H_3L^+$ and $H_4L^{2+}$) assume the same conformation in the crystal, thus resulting in symmetry equivalence and making it impossible to assign a different degree of protonation. On the other hand, the [3333] macrocyclic conformation preorganizes the donor atoms in a square planar geometry suitable for metal ion coordination and in the two Cu(II) complexes, the cation has an almost perfect square pyramidal coordination environment with the apical position occupied by a water oxygen atom ($[Cu(H_2L)(H_2O)](ClO_4)_2{\cdot}10.46H_2O$) or a chloride anion ($[Cu(H_2L)Cl]Cl{\cdot}3H_2O$) (Table S2†).

Notably, the [3333] conformation determines the position of the methyl carbon atoms and of the first carbon atoms in the pendant arms, which occupy almost the same position above the mean plane defined by the four nitrogen atoms in all structures. The conformational rigidity given by the small and preorganized macrocycle also partially affects the pendant arms, which have the first C–C dihedrals in the more stable *trans* conformation. Nevertheless, as shown in Fig. S2,† the rotatable torsions can be affected by environment and packing forces so that while in the more hydrated $(H_3L)(H_4L)(ClO_4)_3{\cdot}11H_2O$ and $[Cu(H_2L)(H_2O)](ClO_4)_2{\cdot}10.46H_2O$, $H_2L$ assumes very similar conformations, in $(H_5L)(ClO_4)_3{\cdot}2H_2O$ and $[Cu(H_2L)Cl]Cl{\cdot}3H_2O$, the nitroso pyrimidine groups are differently oriented.

In fact, the molecular symmetry of $H_2L$ can be analysed in terms of the $N–C–C–N_{amide}$ torsion angular values along the pendant arms. In $(H_3L)(H_4L)(ClO_4)_3{\cdot}11H_2O$ and $[Cu(H_2L)(H_2O)](ClO_4)_2{\cdot}10.46H_2O$, the $N–C–C–N_{amide}$ features a *±gauche/trans/−gauche* sequence, which is associated with the presence of a 2-fold rotational axis passing through the centre of the N4 plane and normal to it. In $(H_5L)(ClO_4)_3{\cdot}2H_2O$, the molecular symmetry is better described as Cs, the mirror plane being normal to the N4 plane and containing the two methyl C–N bonds. The $N–C–C–N_{amide}$ dihedral sequence is *±gauche/trans/+gauche*, resulting in convergent nitroso groups and in the formation of a supramolecular macrocycle held together by two strong N═O–H···O═N H-bonds. On the other hand, in $[Cu(H_2L)Cl]Cl{\cdot}3H_2O$ only one of the pendant arms has the C–C bond in *trans* conformation, while in the other, the C–C bond is of the *gauche* type (Fig. 5). These findings evidence that the complexed ligand can have enough mobility to rearrange itself and place the nitroso pyrimidine groups in contact with the surface of carbon nanotubes, while at the same time having the metal centre exposed to the solvent and available for binding or interaction with exogenous species. Interestingly, preliminary molecular dynamics simulations (empirical force-field method) carried out to study the interaction of the [($H_2L$)

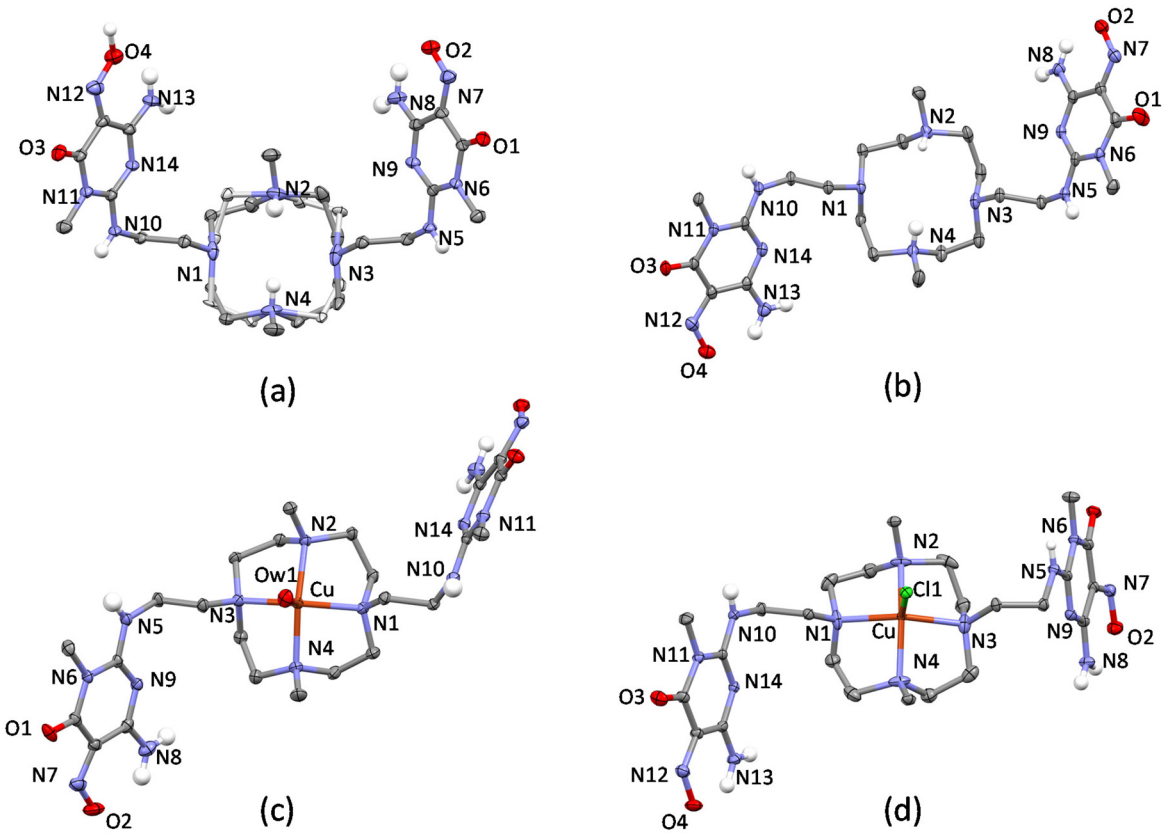


**Fig. 4** $H_2L$ ligand or $Cu(H_2L)^{2+}$ complex in (a) $(H_5L)(ClO_4)_3{\cdot}2H_2O$ (both disordered conformers are shown), (b) $(H_3L)(H_4L)(ClO_4)_3{\cdot}11H_2O$, (c) $[Cu(H_2L)(H_2O)](ClO_4)_2{\cdot}10.46H_2O$ and (d) $[Cu(H_2L)Cl]Cl{\cdot}3H_2O$ crystal structures (non-polar H atoms are omitted for clarity).

$Pd]^{2+}$ complex with a graphene slice, as a model for the MWCNT, gave both the nitroso pyrimidine groups stacked on the graphene and *gauche*/*gauche*/*gauche* sequence for the N–C–C–$N_{amide}$ dihedrals (Fig. S3†).

Concerning the crystal structure of $[Pd(\mathbf{1})]Cl_2{\cdot}4H_2O$, the asymmetric unit contains two not symmetry equivalent $[Pd(\mathbf{1})]^{2+}$ complexes, which differ from each other only for the relative arrangement of the sulfonamide moieties of the pendant arms (Fig. S4†). The ORTEP-like drawing of the two Pd(II) complexes (Fig. 6) clearly shows that the cyclen unit assumes the same [3333] conformation found in the crystals of protonated and Cu(II)-complexed $H_2L$ and that Pd(II) and Cu(II) ions are coordinated by the tetraazamacrocycle in an almost equivalent manner. The deviation from planarity of the four nitrogen atoms is at most 0.025 Å in the four metal complexes (two Cu(II) complexes and two not symmetry equivalent Pd(II) complexes). The Cu(II) ions are shifted from the basal plane toward the apical position by 0.4882(6) Å in $[Cu(H_2L)(H_2O)](ClO_4)_2{\cdot}10.46H_2O$ and by 0.5417(4) Å in $[Cu(H_2L)Cl]Cl{\cdot}3H_2O$, while in the case of the Pd(II) complexes, the deviations from the mean planes are 0.3835(9) Å (Pd1) and 0.378(1) Å (Pd2). It is worth noting that in both Pd(II) complexes, a pendant arm places its nitrogen atom at about 3 Å from the metal ion (Table S3†), suggesting long-distance occupation of the fifth position of a strongly distorted square pyramid. This hypothesis is confirmed by the position of the amidic hydrogen atom found in the Fourier difference map for one of the two complexes and by the corresponding C–N–S bond angle (116.2(8)°, Fig. 6b), which are in agreement with the presence of a $sp^3$ nitrogen atom with the lone pair available for coordination. This finding is in line with the theoretical calculations[35]

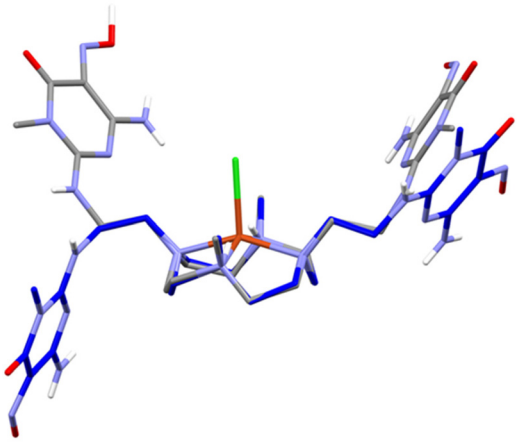

**Fig. 5** Superposition of the $H_2L$ ligands in the crystal structure of $(H_5L)(ClO_4)_3{\cdot}2H_2O$ (gray, only the prevalent conformer is shown) and $[Cu(H_2L)Cl]Cl{\cdot}3H_2O$ (blue).

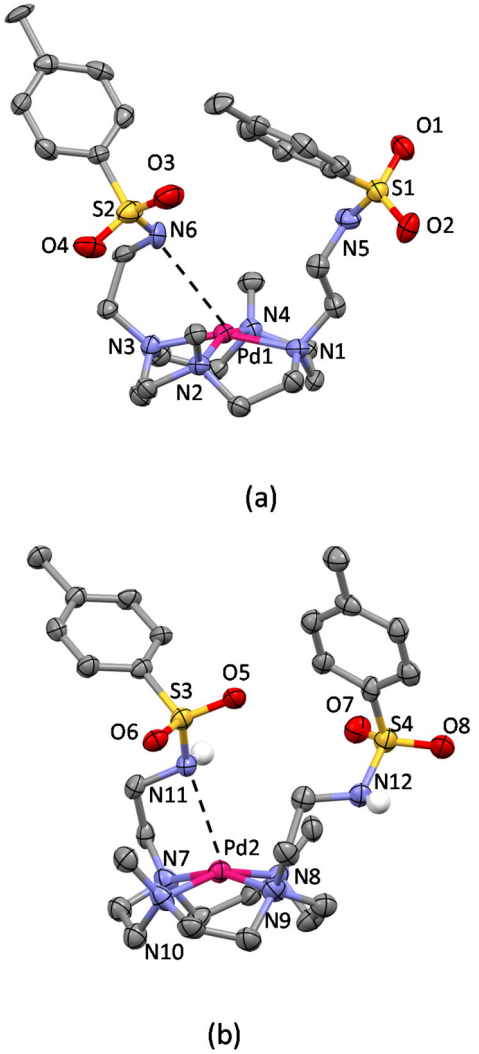


**Fig. 6** Not symmetry equivalent $[Pd(\mathbf{1})]^{2+}$ complexes in the asymmetric unit of the $[Pd(\mathbf{1})]Cl_2{\cdot}4H_2O$ crystal structure. (a) Mol A and (b) mol B (non-polar hydrogen atoms are omitted for clarity).

already mentioned showing that $O_2$ is able to form an apical bond with Pd(II) centres. Indeed, despite the known propensity of Pd(II) to square planar coordination, it is possible to recover almost 150 structures from the Cambridge Structural Database showing a possibly five-coordinated Pd(II) ion, almost half of them showing the metal in a distorted square pyramidal environment. For those having a nitrogen atom in the apical position, the Pd–N bond distances range from 2.2 to 2.9 Å.[59]

### SEM and XPS characterization of the catalyst

The SEM images of MWCNT, MWCNT-L and MWCNT-LPd (Fig. S5†) show homogeneous networks of carbon nanotubes with no marked differences in the morphology of the three samples. In the relevant EDS (SEM-energy-dispersive spectroscopy) spectra (Fig. S6†), pristine MWCNTs show only the C signal and a minimal presence of oxygen, in accordance with the specifications provided by the supplier, whereas in the case of MWCNT-L, there is also the N signal, due to the presence of the ligand, and the MWCNT-LPd catalyst shows a Pd loading of about 1.5% by weight in good agreement with the catalyst preparation data (1.71%) reported above. The EDS map of MWCNT-LPd (Fig. 7) shows that Pd is uniformly distributed over the sample, evidencing that the supramolecular approach adopted for the preparation of the catalyst successfully leads to a homogeneous distribution of the catalytic centres. Chloride, which is expected to be present as the counter-ion of coordinated Pd(II) ions, is also detected in the EDS analysis (Fig. 7d) as well as in the XPS spectra (Fig. S7†).

XPS analysis of MWCNT-LPd, focused on the Pd region and Pd oxidation state (3d transition of palladium, binding energy from 360 eV to 325 eV), shows that the metal is mainly present as Pd(II). Peak fitting reveals that the sample contains a small amount (*ca.* 12%) of PdO/C. In Fig. S7b,† the Pd1 component corresponds to $Pd(II)/H_2L$ (binding energy $3d_{5/2}$ = 338.8 eV, $3d_{3/2}$ = 344.1 eV)[60] while the Pd2 component corresponds to PdO/C (binding energy $3d_{5/2}$ = 336.3 eV, $3d_{3/2}$ = 341.5 eV).[61,62] No component of the reduced metal Pd(0) was found. Similar behaviour was shown by analogous systems,[28] and it is perhaps connected to the preparation method and/or reducing character of the leftover C impurities or Pd interactions with surface defects.[34]

### Electrochemical evaluation of the catalytic performance in the ORR

The evaluation of the catalytic activity of electrocatalysts in the ORR was carried out with reference to the three parameters: the onset potential ($E_{on}$), the half-wave potential ($E_{1/2}$) and the number of exchanged electrons ($n$).[63] The onset potential represents the limit value at which the ORR starts to evolve in significant current density values. In this work, the onset potential is defined as the potential at which the current density reaches a value of −0.1 mA $cm^{-2}$ (black dotted line, Fig. 8). Note that a more positive potential corresponds to a lower barrier for the ORR.[64] The half-wave potential ($E_{1/2}$) is the potential to reach half the limiting current density obtained from the LSV curve, and it is a widely accepted indicator for evaluating the ORR performance.[65,66] Indeed, the $E_{1/2}$ in the mixed controlled region of LSV curves reflects the coupling behaviour of surface reaction and mass diffusion.[63] The third important parameter, the number of exchanged electrons ($n$), allows the assessment of the principal reaction pathway in the ORR. A catalyst should preferably promote a four-electron exchange leading to the formation of $H_2O$ and prevent a two-electron exchange producing $H_2O_2$ to avoid the negative influence of the latter on the yields of the ORR process and the corrosive effects it has on the membrane used in fuel cells.[67,68]

We studied the electrochemical behaviour of MWCNT-LPd by cyclic voltammetry in 0.1 M KOH purged with either $N_2$ or $O_2$. Cyclic voltammograms (CVs) of the modified electrode are shown in Fig. S8.† In all cases, a sharp and irreversible peak of oxygen reduction is observed in the presence of $O_2$, which is not present when the environment is saturated with $N_2$. The ORR peak current signal shows a higher density peak current

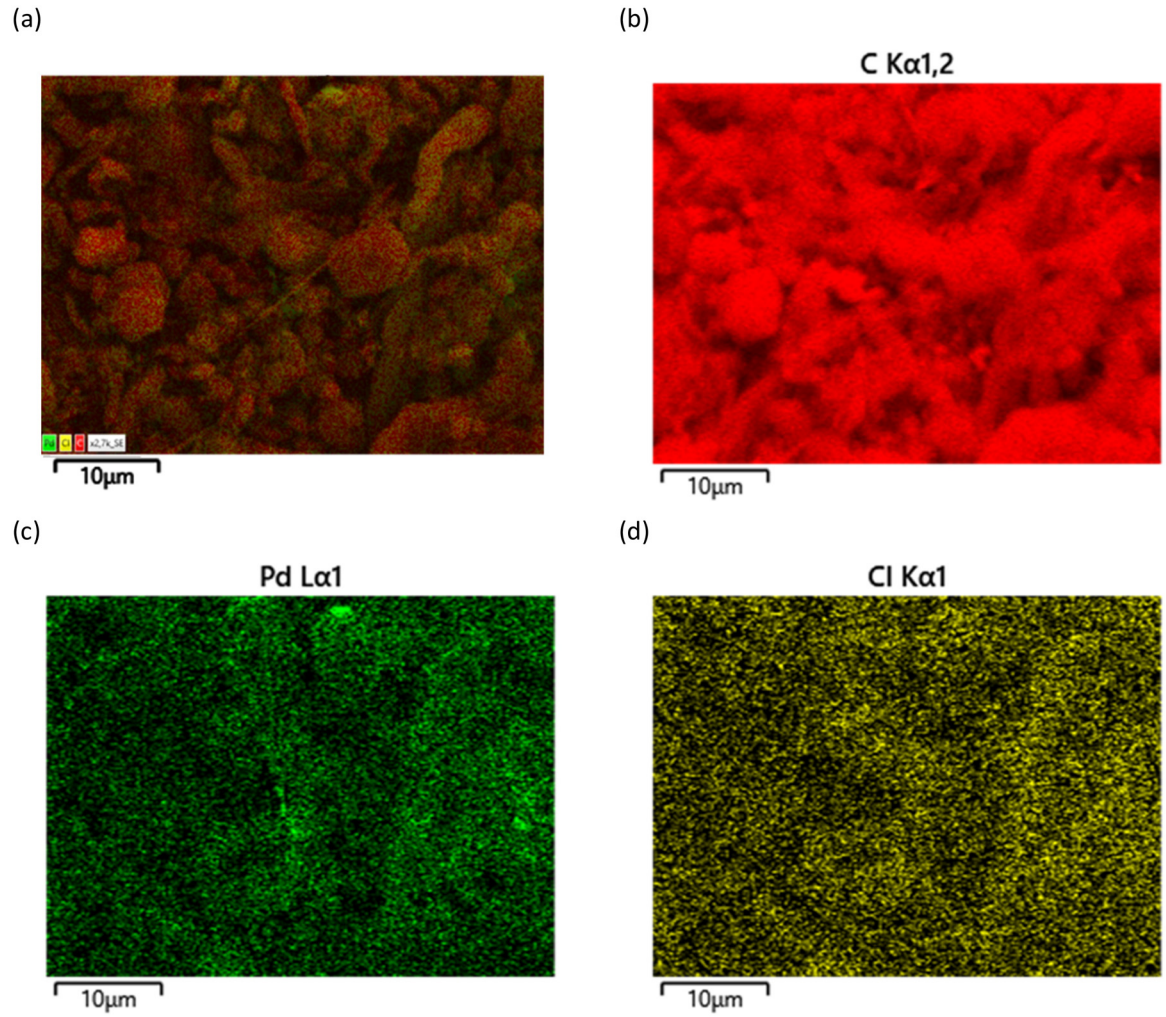


**Fig. 7** EDS mapping of MWCNT-LPd: (a) EDS layered image, (b) C signals, (c) Pd signals, and (d) Cl signals.

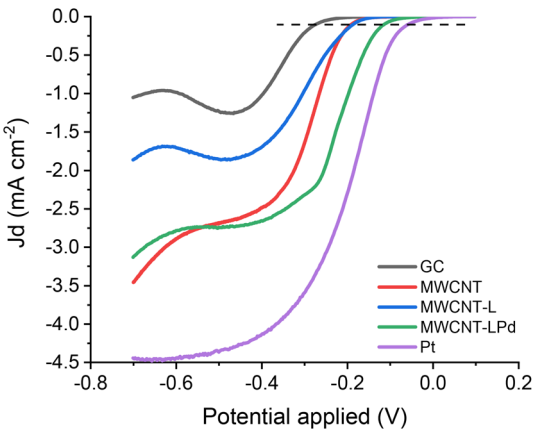


**Fig. 8** ORR electrocatalytic performance, LSV 1600 rpm rotation rate, and 5 mV $s^{-1}$ scan rate in KOH 0.1 M $O_2$ saturated solution. RRDE disk current densities of the modified GC electrode and the benchmark electrode. The horizontal dotted line at a current density of −0.1 mA $cm^{-2}$ shows the onset potential of samples.

with Pd-containing catalysts, confirming the catalytic activity of this complexed metal ion. CVs of MWCNT-L and MWCNT-LPd also show a redox couple at the potential of −0.3 V and −0.4 V, respectively, which is present both in $O_2$ and $N_2$ purged solutions, while only capacitive currents are observed in the same potential range for MWCNTs and the benchmark GC electrode (compare Fig. S8a–d†). The redox couple of the $H_2L$ ligand may play an important role in the ORR electron transfer phenomena,[35] and the influence of the redox couple on the electron transfer involved in the ORR process is still being studied.

Fig. 8 shows the ORR polarization curves recorded at 1600 rpm for each sample at a potential scan rate of 5 mV $s^{-1}$ in a KOH 0.1 M oxygen saturated solution. The polarization curves for the bare GC electrode, Pt electrode, as well as the GC electrode functionalized with pristine MWCNTs and MWCNT-L (same functionalization method) are also reported. The horizontal dotted line at the current density of −0.1 mA $cm^{-2}$ shows the onset potential of the samples.

**Table 2** Catalytic performances of the modified glassy carbon electrode and the benchmark electrode

| Electrode | $E_{on}$ [a] (V) | $E_{1/2}$ [b] (V) | $n$ [c] | % $H_2O_2$ [d] |
|---|---|---|---|---|
| GC | −0.276 | −0.354 | 2.16 | 91.7 |
| MWCNT | −0.191 | −0.284 | 2.43 | 78.31 |
| MWCNT-$H_2$L | −0.187 | −0.298 | 2.07 | 96.6 |
| MWCNT-$H_2$L-Pd(II) | −0.112 | −0.222 | 3.70 | 15.0 |
| Pt | −0.059 | −0.198 | 3.79 | 10.7 |

[a] Onset potential *vs.* Ag/AgCl KCl sat. [b] Half-wave potential calculated at the half of the limiting current density obtained from the LSV curve. [c] Number of exchanged electrons per $O_2$ molecule, the value at −0.35 V calculated with an experimentally determined collection efficiency number (reported in Fig. S10†). [d] Percentage of hydrogen peroxide calculated from the value of $n$.

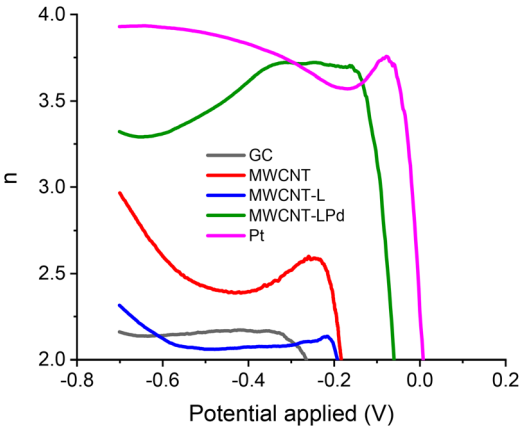


**Fig. 9** Dependency of the RRDE number of exchanged electrons per $O_2$ molecule *vs.* the LSV scanning potential values.

Table 2 provides the electrochemical results for all systems.

As displayed in Fig. 8, the catalytic activities, in terms of both $E_{on}$ and current values, increase depending on the catalyst nature in the order: bare GC < pristine MWCNTs ≈ MWCNT-L < MWCNT-LPd < bare Pt electrode. This evidence rules out significant catalytic properties of the MWCNT-supported substrate and ligands, while highlighting the prominent role of Pd(II) in enhancing the catalytic activity. The $E_{on}$ values observed for MWCNT-LPd are close to the benchmark values obtained under the same conditions with a commercial Pt working electrode: the $E_{on}$ value for MWCNT-LPd is only 53 mV less positive than that observed for the Pt electrode (Table 2). The same trend is followed by the half-wave potentials ($E_{1/2}$, Table 2).

In order to provide the number of exchanged electrons and investigate the reaction pathway of the ORR during the RRDE LSV measurements, the Pt ring electrode was held at a potential of +0.50 V to ensure the complete oxidation of $H_2O_2$ eventually produced at the modified GC disk electrode. The ring disk current densities in $N_2$ and $O_2$ saturated KOH solutions are shown in Fig. S9.† Background currents (under $N_2$ saturated conditions) have been used to account for capacitive current contribution.

RRDE calibration with $K_3Fe(CN)_6$ was used to determine the experimental collection efficiency ($N$) for each modified GC electrode, so that accurate values for the number of exchanged electrons could be derived.[69] Fig. S10† shows the LSV ring-disk current; the collection efficiency values are very close to the theoretical value (38.3%). The number of exchanged electrons per $O_2$ molecule ($n$) as a function of the potential applied at the RRDE working electrode is presented in Fig. 9. As can be seen in this figure, this number ($n$) is very close to 4 for the MWCNT-LPd catalyst, especially in the onset potential region, signifying an almost exclusive conversion of $O_2$ into $H_2O$.

The measured ring and disk currents for MWCNT-LPd at the suggested potential of −0.35 V demonstrate that, under the said conditions, the direct conversion to $H_2O$ reaches 85.0%, compared to 89% of the Pt electrode (Table 2).

Quite different results are instead obtained in the case of the GC electrode used as a benchmark, MWCNT and MWCNT-L, the latter giving an exchanged electron number close to 2, thus a predominant formation of hydrogen peroxide.

Further characterization of the half-cell with MWCNT-LPd was performed by using the RRDE in galvanostatic mode to simulate a working fuel cell at a fixed potential. The modified GC disk electrode potential was held at −0.60 V and the ring electrode was held at +0.50 V, respectively, for 600 s at 1600 rpm. The galvanostatic results shown in Fig. S11† also provide a short-time stability test. The ring-disk current density values remain constant during the analysis, indicating the robustness of the catalyst. The time-averaged number of exchanged electrons per $O_2$ molecule shows that direct conversion to water is the main process during the evolution of time. Nevertheless, further investigation is needed to evaluate the long-term stability of the catalyst for fuel-cell applications.

## Conclusions

The main objective of this work was to ascertain whether the ability of Pd(II) to function as a catalyst in the oxygen reduction reaction (ORR) in alkaline aqueous solutions is strictly connected to the presence of readily available coordination sites in the square planar coordination geometry typical of this metal ion. This objective is intended as an experimental verification of previous theoretical results showing that Pd(II) can still function as an efficient catalyst for ORR through the axial interaction of $O_2$ with metal centres.[35] Beyond its conceptual value, this objective has great relevance for the design and synthesis of ligands used to anchor Pd(II) in heterogeneous catalysts. The possibility of using macrocyclic ligands that saturate the square planar coordination environment typical of this metal ion, without the need to preserve coordination sites occupied by labile donors, greatly facilitates the preparation of these ligands and allows for stronger coordination of the metal ion with consequent enhancement of the catalyst robustness.

The results obtained in the present work using a Pd(II) complex anchored on MWCNTs in which the square planar coordinative geometry of the metal ion is saturated by the four nitrogen atoms of a tetraazacycloalkane leave no room for doubt about the ability of Pd(II) to function very well as a catalyst in the ORR even under similar conditions. Indeed, the new MWCNT-LPd catalyst has an onset potential ($E_{on}$) which is only 53 mV less positive than that of a commercial Pt electrode, and the same trend is followed by the half-wave potentials ($E_{1/2}$ is only 24 mV less positive than that observed for the Pt electrode). The number of exchanged electrons per $O_2$ molecule is very close to 4, especially in the onset potential region, denoting an almost exclusive conversion of $O_2$ into $H_2O$. Ring and disk currents measured at the potential of −0.35 V demonstrate that, under the said conditions, the direct conversion to $H_2O$ reaches 85.0%, compared to 89% of the Pt electrode. Furthermore, a short-term test (600 s) conducted on the half-cell with MWCNT-LPd in galvanostatic mode to simulate a fuel cell operating at a fixed potential demonstrated that the catalyst is very robust in this time interval: the current density remained constant during the analysis and the time-averaged number of electrons exchanged per $O_2$ molecule showed that the direct conversion to water was maintained throughout. Remarkably, these results were obtained with a heterogeneous catalyst containing only 1.72% by weight of the precious metal (Pd) homogeneously distributed over the surface of the solid support (MWCNTs).

## Conflicts of interest

There are no conflicts to declare.

## Acknowledgements

Project 2022NW4P2T CUP B53D23013890006 “From metal nanoparticles to molecular complexes in electrocatalysis for green hydrogen evolution and simultaneous fine chemicals production” PRIN2022 Progetti di Ricerca di Rilevante Interesse Nazionale funded by the Italian Ministry of University and Research and NextGenerationEU is acknowledged.

## References

1 *Fuel Cell Technology Handbook*, ed. G. Hoogers and F. Kreith, CRC Press, Boca Raton, 2002.
2 B. C. H. Steele and A. Heinzel, *Nature*, 2001, **414**, 345–352.
3 X. He, S. Minelli, A. Vertova and A. Minguzzi, *Curr. Opin. Electrochem.*, 2022, **36**, 101166.
4 J. Hou, M. Yang, C. Ke, G. Wei, C. Priest, Z. Qiao, G. Wu and J. Zhang, *EnergyChem*, 2020, **2**, 100023.
5 J. K. Nørskov, J. Rossmeisl, A. Logadottir, L. Lindqvist, J. R. Kitchin, T. Bligaard and H. Jónsson, *J. Phys. Chem. B*, 2004, **108**, 17886–17892.
6 F. Nosheen, T. Anwar, A. Siddique and N. Hussain, *Front. Chem.*, 2019, **7**, 456.
7 I. Staffell, D. Scamman, A. Velazquez Abad, P. Balcombe, P. E. Dodds, P. Ekins, N. Shah and K. R. Ward, *Energy Environ. Sci.*, 2019, **12**, 463–491.
8 M. Kiani, X. Q. Tian and W. Zhang, *Coord. Chem. Rev.*, 2021, **441**, 213954.
9 X. Huang, Y. Wang, W. Li and Y. Hou, *Sci. China: Chem.*, 2017, **60**, 1494–1507.
10 H. A. Miller, M. Bevilacqua, J. Filippi, A. Lavacchi, A. Marchionni, M. Marelli, S. Moneti, W. Oberhauser, E. Vesselli, M. Innocenti and F. Vizza, *J. Mater. Chem. A*, 2013, 13337–13347.
11 P. Jiao, D. Ye, C. Zhu, S. Wu, C. Qin, C. An, N. Hu and Q. Deng, *Nanoscale*, 2022, **14**, 14322–14340.
12 M. D. Bhatt and J. Y. Lee, *Energy Fuels*, 2020, **34**, 6634–6695.
13 X. Li, G. Liu, H. Zheng, K. Sun, L. Wan, J. Cao, S. Asif, Y. Cao, W. Si, F. Wang and A. Bokhari, *Energies*, 2023, **16**, 128.
14 D. Iglesias, A. Giuliani, M. Melchionna, S. Marchesan, A. Criado, L. Nasi, M. Bevilacqua, C. Tavagnacco, F. Vizza, M. Prato and P. Fornasiero, *Chem*, 2018, **4**, 106–123.
15 G. Tuci, C. Zafferoni, A. Rossin, A. Milella, L. Luconi, M. Innocenti, L. Truong Phuoc, C. Duong-Viet, C. Pham-Huu and G. Giambastiani, *Chem. Mater.*, 2014, **26**, 3460–3470.
16 Z. Yan, L. Gao, C. Dai, M. Zhang, X. Lv and P. K. Shen, *Int. J. Hydrogen Energy*, 2018, **43**, 3705–3715.
17 (*a*) L. Yan, P. Li, Q. Zhu, A. Kumar, K. Sun, S. Tian and X. Sun, *Chem*, 2023, **9**, 280–342; (*b*) A. Kumar, S. Ibraheem, T. A. Nguyen, R. K. Gupta, T. Maiyalagan and G. Yasin, *Coord. Chem. Rev.*, 2021, **446**, 214122; (*c*) A. Kumar, Y. Zhang, W. Liu and X. Sun, *Coord. Chem. Rev.*, 2020, **402**, 213047; (*d*) A. Kumar, V. K. Vashistha and D. K. Das, *Coord. Chem. Rev.*, 2021, **431**, 213678.
18 M. Wang, H. Zhang, Y. Liu and Y. Pan, *J. Energy Chem.*, 2022, **72**, 56–72.
19 S. Ji, Y. Chen, X. Wang, Z. Zhang, D. Wang and Y. Li, *Chem. Rev.*, 2020, **120**, 11900–11955.
20 B. Singh, V. Sharma, R. P. Gaikwad, M. B. Gawande, P. Fornasiero, R. Zboril and R. Zboril, *Small*, 2021, **17**, e2006473.
21 H. W. Kim, M. B. Ross, N. Kornienko, L. Zhang, J. Guo, P. Yang and B. D. McCloskey, *Nat. Catal.*, 2018, **1**, 282–290.
22 J. K. Edwards, S. J. Freakley, R. J. Lewis, J. C. Pritchard and G. J. Hutchings, *Catal. Today*, 2015, **248**, 3–9.
23 A. Goti and F. Cardona, Hydrogen peroxide in green oxidation reactions: Recent catalytic processes, in *Green Chemical Reactions*, ed. P. Tundo and V. Esposito, Springer, Berlin/Heidelberg, 2008, pp. 191–212.
24 A. Gómez-Marín, J. Feliu and T. Edson, *ACS Catal.*, 2018, **8**, 7931–7943.
25 L. Gubler, S. M. Dockheer and W. H. Koppenol, *J. Electrochem. Soc.*, 2011, **158**, B755.
26 M. Passaponti, M. Savastano, M. P. Clares, M. Inclán, A. Lavacchi, A. Bianchi, E. García-España and M. Innocenti, *Inorg. Chem.*, 2018, **57**, 14484–14488.

 

27 US Department of Energy: Office of Energy Efficiency and Renewable Energy. https://www.energy.gov/eere/fuelcells/doe-technical-targets-polymer-electrolyte-membrane-fuel-cell-components.
28 M. Savastano, M. Passaponti, W. Giurlani, L. Lari, A. Bianchi and M. Innocenti, *Energies*, 2020, **13**, 5539.
29 (*a*) M. Savastano, M. Passaponti, W. Giurlani, L. Lari, N. Calisi, E. Delgado-Pinar, E. S. Serrano, E. Garcia-España, M. Innocenti, V. K. Lazarov and A. Bianchi, *Inorg. Chim. Acta*, 2021, **518**, 120250; (*b*) M. Savastano, C. Zoppi, A. Bianchi and C. Bazzicalupi, *Inorg. Chim. Acta*, 2020, **511**, 119793.
30 Q. An, S. Bo, J. Jiang, C. Gong, H. Su, W. Cheng, Q. Liu and W. Cheng, *Adv. Sci.*, 2023, **10**, 2205031.
31 R. Majee, S. Parvin, Q. A. Islam, A. Kumar, B. Debnath, S. Mondal, S. Bhattacharjee, S. Das, A. Kumar and S. Bhattacharyya, *Chem. Rec.*, 2022, **22**, 202200070.
32 W. Xu, Y. Sun, J. Zhou, M. Cao, J. Luo, H. Mao, P. Hu, H. Gu, H. Zhai, H. Shang and Z. Cai, *Nano Res.*, 2023, **16**, 2294–2301.
33 M. Savastano, P. Arranz-Mascarós, C. Bazzicalupi, M. P. Clares, M. L. Godino-Salido, M. D. Gutiérrez-Valero, M. Inclán, A. Bianchi, E. García-España and R. López-Garzón, *J. Catal.*, 2017, **353**, 239–249.
34 (*a*) A. M. Valbuena-Rus, M. Savastano, P. Arranz-Mascarós, C. Bazzicalupi, M. P. Clares, M. L. Godino-Salido, M. D. Gutiérrez-Valero, M. Inclán, A. Bianchi, E. García-España and R. López-Garzón, *Inorg. Chem.*, 2022, **61**, 12610–12624; (*b*) M. Savastano, P. Arranz-Mascarós, M. P. Clares, R. Cuesta, M. L. Godino-Salido, L. Guijarro, M. D. Gutiérrez-Valero, M. Inclán, A. Bianchi, E. García-España and R. López-Garzón, *Molecules*, 2019, **24**, 2714.
35 M. Bonechi, W. Giurlani, M. Vizza, M. Savastano, A. Stefani, A. Bianchi, C. Fontanesi and M. Innocenti, *Catalysts*, 2021, **11**, 764.
36 N. J. Low, M. D. López, P. Arranz, J. Cobo, M. L. Godino, R. López, M. D. Gutiérrez, M. Melguizo, G. Ferguson and C. Glidewell, *Acta Crystallogr., Sect. B: Struct. Sci.*, 2000, **56**, 882–892.
37 M. Savastano, V. Monini, C. Bazzicalupi and A. Bianchi, *Inorganics*, 2022, **10**, 12.
38 C. Bazzicalupi, A. Bianchi, T. Biver, C. Giorgi, S. Santarelli and M. Savastano, *Inorg. Chem.*, 2014, **53**, 12215–12224.
39 M. Fontanelli and M. Micheloni, Proceedings of the Ist Spanish-Italian Congress on Thermodynamics of Metal Complexes. Diputación de Castellón, Castellón, Spain, 1990, pp. 41–43.
40 M. Savastano, M. Fiaschi, G. Ferraro, P. Gratteri, P. Mariani, A. Bianchi and C. Bazzicalupi, *Molecules*, 2020, **25**, 1355.
41 G. Gran, *Analyst*, 1952, **77**, 661–671.
42 P. Gans, A. Sabatini and A. Vacca, *Talanta*, 1996, **43**, 1739–1753.
43 J. García-Martín, R. López-Garzón, M. L. Godino-Salido, M. D. Gutiérrez-Valero, P. Arranz-Mascarós, R. Cuesta and F. Carrasco-Marín, *Langmuir*, 2005, **21**, 6908–6914.
44 Experiments in Analytical Electrochemistry The Care and Feeding of Electrodes. https://www.semanticscholar.org/paper/Experiments-in-Analytical-Electrochemistry-The-Care/1d6b28acd37f31f270fdf6da081a369b7bb9c176.
45 A. J. Bard, L. R. Faulkner and H. S. White, *Electrochemical Methods: Fundamentals and Applications*, Wiley, New York, 2nd edn, 2020.
46 M. Passaponti, L. Rosi, M. Savastano, W. Giurlani, H. A. Miller, A. Lavacchi, J. Filippi, G. Zangari, F. Vizza and M. Innocenti, *J. Power Sources*, 2019, **427**, 85–90.
47 U. A. Paulus, T. J. Schmidt, H. A. Gasteiger and R. J. Behm, *J. Electroanal. Chem.*, 2001, **495**, 134–145.
48 *Rotating Electrode Methods and Oxygen Reduction Electrocatalysts*, ed. X. Wei, G. Yin and J. Zhang, Elsevier, 2014.
49 C. Song and J. Zhang, Electrocatalytic Oxygen Reduction Reaction, in *PEM Fuel Cell Electrocatalysts and Catalyst Layers*, ed. J. Zhang, Springer, London, 2008.
50 G. Maccaferri, C. Zanardi, Z. Y. Xia, A. Kovtun, A. Liscio, F. Terzi, V. Palermo and R. Seeber, *Carbon*, 2017, **120**, 165–175.
51 C. Borri, N. Calisi, E. Galvanetto, N. Falsini, F. Biccari, A. Vinattieri, G. Cucinotta and S. Caporali, *Nanomaterials*, 2020, **10**, 60.
52 D. A. Shirley, *Phys. Rev. B: Solid State*, 1972, **5**, 4709–4714.
53 *SADABS*, Bruker AXS Inc., Madison (WI), USA, 2001.
54 G. M. Sheldrick, *Acta Crystallogr., Sect. A: Found. Adv.*, 2015, **71**, 3–8.
55 G. M. Sheldrick, *Acta Crystallogr., Sect. C: Struct. Chem.*, 2015, **71**, 3–8.
56 C. F. Macrae, I. Sovago, S. J. Cottrell, P. T. A. Galek, P. McCabe, E. Pidcock, M. Platings, G. P. Shields, J. S. Stevens, M. Towler and P. A. Wood, *J. Appl. Crystallogr.*, 2020, **53**, 226–235.
57 R. López-Garzón, M. L. Godino-Salido, M. D. Gutiérrez-Valero, P. Arranz-Mascarós, M. Melguizo, C. García, M. Domingo-García and F. J. López-Garzón, *Inorg. Chim. Acta*, 2014, **417**, 208–221.
58 J. Dale, *Acta Chem. Scand.*, 1973, **27**, 1115–1129.
59 (*a*) T. J. Hubin, N. W. Alcock and D. H. Busch, *Acta Crystallogr., Sect. C: Cryst. Struct. Commun.*, 1999, **55**, 1404–1406; (*b*) M. Rimoldi, F. Ragaini, E. Gallo, F. Ferretti, P. Macchi and N. Casati, *Dalton Trans.*, 2012, **41**, 3648–3658; (*c*) M. Kujime, S. Hikichi and M. Akita, *Chem. Lett.*, 2003, **32**, 486–487; (*d*) J. R. Khusnutdinova, N. P. Rath and L. M. Mirica, *Angew. Chem., Int. Ed.*, 2011, **50**, 5532–5536; (*e*) K. Wieghardt, E. Schoffmann, B. Nuber and J. Weiss, *Inorg. Chem.*, 1986, **25**, 4877–4883; (*f*) T. Sakai, Z. Taira, S. Yamazaki and T. Ama, *Polyhedron*, 1989, **8**, 1989–1993; (*g*) E. C. Constable, S. M. Elder, J. Healy, M. D. Ward and D. A. Tocher, *J. Am. Chem. Soc.*, 1990, **112**, 4590–4592; (*h*) J. R. Khusnutdinova, N. P. Rath and L. M. Mirica, *Inorg. Chem.*, 2014, **53**, 13112–13129; (*i*) M. Kujime, S. Hikichi and M. Akita, *Organometallics*, 2001, **20**, 4049–4060; (*j*) K. Yamamoto, J. Li, J. A. O. Garber, J. D. Rolfes, G. B. Boursalian, J. C. Borghs, C. Genicot, J. Jacq, M. van Gastel, F. Neese and T. Ritter, *Nature*, 2018, **554**, 511–514; (*k*) J. Luo, N. P. Rath and L. M. Mirica, *Organometallics*,

2013, **32**, 3343–3353; (*l*) M. Broring and C. D. Brandt, *Chem. Commun.*, 2003, 2156–2157.
60 NIST **https://srdata.nist.gov/xps/XPSDetailPage.aspx?AllDataNo=28665#Citation.htm**.
61 NIST **https://srdata.nist.gov/xps/XPSDetailPage.aspx?AllDataNo=29100**.
62 NIST **https://srdata.nist.gov/xps/XPSDetailPage.aspx?AllDataNo=66751**.
63 J. Wang, C.-X. Zhao, J.-N. Liu, D. Ren, B.-Q. Li, J.-Q. Huang and Q. Zhang, *Nano Mater. Sci.*, 2021, **3**, 313–318.
64 Y.-F. Xia, P. Guo, J.-Z. Li, L. Zhao, X.-L. Sui, Y. Wang and Z.-B. Wang, *iScience*, 2021, **24**, 103024.
65 A. Brouzgou, S. Song, Z.-X. Liang and P. Tsiakaras, *Catalysts*, 2016, **6**, 159.
66 X. Ge, A. Sumboja, D. Wuu, T. An, B. Li, F. W. T. Goh, T. S. A. Hor, Y. Zong and Z. Liu, *ACS Catal.*, 2015, **5**, 4643–4667.
67 X. Zhao and Y. Liu, *J. Am. Chem. Soc.*, 2021, **143**, 9423–9428.
68 S. Zaman, L. Huang, A. I. Douka, H. Yang, B. You and B. Y. Xia, *Angew. Chem., Int. Ed.*, 2021, **60**, 17832–17852.
69 M. Passaponti, L. Lari, M. Bonechi, F. Bruni, W. Giurlani, G. Sciortino, L. Rosi, L. Fabbri, M. Vizza, V. K. Lazarov, C. Fontanesi and M. Innocenti, *Energies*, 2020, **13**, 5646.